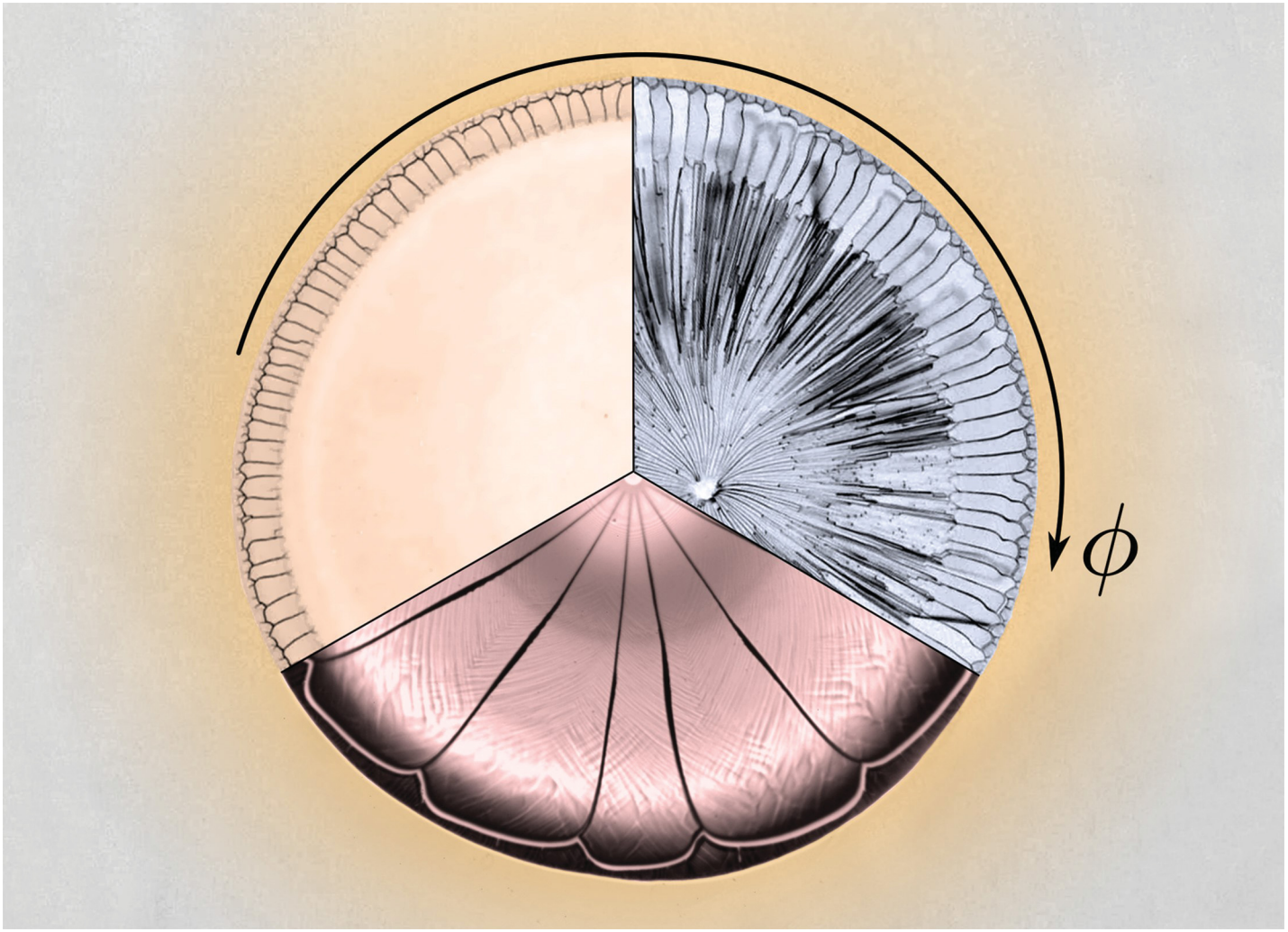

Highlighting research from the Hatsopoulos Microfluids Laboratory at MIT.

Crack morphologies in drying suspension drops

Drops of aqueous suspensions of nanoparticles placed on a substrate form a solid deposit as they dry. The initial concentration of particles governs both the shape of the deposit and the crack morphology.

As featured in:

See Philippe Bourrianne, Irmgard Bischofberger *et al.*, *Soft Matter*, 2021, **17**, 8832.

ROYAL SOCIETY OF CHEMISTRY

rsc.li/soft-matter-journal

Registered charity number: 207890

Soft Matter

PAPER

View Article Online
View Journal | View Issue

Cite this: *Soft Matter*, 2021, 17, 8832

Crack morphologies in drying suspension drops†

Philippe Bourrianne, * Paul Lilin, Guillaume Sintès, Traian Nîrca, Gareth H. McKinley and Irmgard Bischofberger *

Received 3rd June 2021,
Accepted 9th September 2021

DOI: 10.1039/d1sm00832c

rsc.li/soft-matter-journal

A drop of an aqueous suspension of nanoparticles placed on a substrate forms a solid deposit as it dries. For dilute suspensions, particles accumulate within a narrow ring at the drop edge, whereas a uniform coating covering the entire wetted area forms for concentrated suspensions. In between these extremes, we report two additional regimes characterized by non-uniform deposit thicknesses and by distinct crack morphologies. We show that both the deposit shape and the number of cracks are controlled exclusively by the initial particle volume fraction. The different regimes share a common avalanche-like crack propagation dynamics, as a result of the delamination of the deposit from the substrate.

Introduction

Thin films of colloidal suspensions in contact with a substrate are prone to failure upon drying.[1–4] As the solvent evaporates, the particles are deposited on the substrate and form a close-packed coating.[5] Stresses build up in this particle deposit and are released through the formation of fractures.[3,5,6] Craquelures in pottery glaze and mud cracks are familiar examples of such thin film failure.[1,7,8] The resulting crack patterns are influenced by the mechanical properties and the history of the material.[9] Understanding these dependences can pave ways to reveal the origin of geological structures[7,10] and can contribute to tracking the original composition of paints as a technique to detect art forgeries.[11] Similarly, when a drop of a concentrated colloidal suspension dries, it leaves a particle-based deposit on the area originally wet by the liquid.[12–14] Radial cracks then form in this discoidal deposit.[12,13,15] Conversely, a drop of a dilute colloidal suspension forms a heterogeneous deposit upon drying, where the particles accumulate at the outer edge of the drop due to a combination of contact line pinning and evaporation-driven flows.[16,17] This phenomenon is the well-known coffee-ring effect.[16] Coffee rings occurring in dilute suspensions and crack patterns occurring in concentrated suspensions illustrate two major limitations for using colloidal suspensions in coating applications: deposit heterogeneity and fragility. Here, we study the transition between coffee rings and discoidal deposits by systematically varying the particle volume fraction. We identify two transitional regimes and show that both the deposit heterogeneity and the crack density are controlled by the initial concentration of particles. We report a critical concentration above which a discoidal deposit is obtained and show that the deposit thickness governs the number of cracks that form. To account for the avalanche-like dynamics observed during crack propagation we suggest a mechanism of delamination as a precursor for fracture.

Department of Mechanical Engineering, Massachusetts Institute of Technology, 77 Massachusetts Avenue, Cambridge, MA, 02139, USA.
E-mail: philippe.bourrianne@princeton.edu, irmgard@mit.edu

† Electronic supplementary information (ESI) available. See DOI: 10.1039/d1sm00832c

Results and discussion

Particle concentration sets crack morphology

We use a colloidal suspension composed of silica nanoparticles (Ludox-AS40, Sigma-Aldrich) of diameter d = 22 nm in water. The particle volume fraction ϕ is varied by diluting the stock solution (40 wt%, ϕ = 22%) with deionized water. Our experiments are performed at ambient temperature T = 22 °C ± 2 °C and relative humidity RH = 27% ± 6%. A 2 μL drop with an initial volume fraction ϕ = 22% deposited on a clean glass slide wets the glass with the same advancing contact angle as water, $\theta = 20° \pm 3°$. The drop adopts a spherical cap shape, as its initial radius R_0 = 1.5 mm is smaller than the capillary length $\kappa^{-1} = \sqrt{\gamma/\rho g} = 2.7$ mm for water, where γ is the interfacial tension and ρ the density of water. As the water evaporates, the spherical cap shrinks and particles are deposited on the glass slide forming a solid deposit, as shown in Fig. 1a. The apparent liquid contact line recedes on this deposit, which results in the formation of a deposit "foot" growing from the drop edge and towards the drop center.[18,19] Water from the liquid spherical cap flows radially outwards in the porous deposit to compensate for evaporation at the deposit interface.[20] These flows cause poroelastic stresses, which are relieved through the

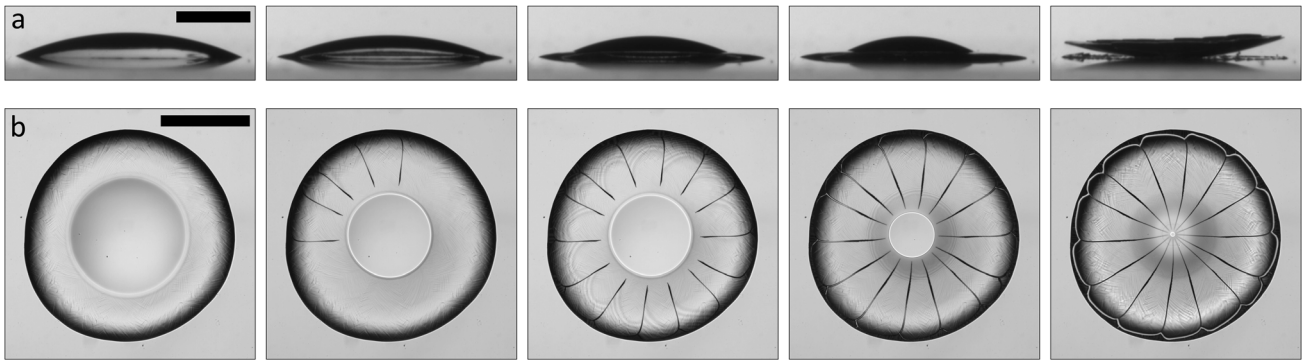

Fig. 1 Drying of colloidal suspension drops with ϕ = 22%. (a) Side view of a 2 μL drop of Ludox suspension drying on a glass slide. From left to right: the liquid initially wets the glass substrate with a contact angle θ = 20°. As the water evaporates, a spherical liquid cap recedes and a layer of close-packed particles is deposited on the glass slide. The deposit eventually cracks and bends during the final stages of drying. The total time is t = 300 s. (b) Bottom view of an 0.3 μL drop of Ludox suspension drying on a glass slide. Particles are deposited at the edge of the drop as the liquid cap recedes towards the center of the drop. Radial cracks form and propagate with an avalanche-like behavior over the deposit, leading to the formation of petals. The scale bars represent 1 mm.

formation of cracks[3,21,22] and by bending of the deposit into a convex structure[12,20,23] (Movie S1, ESI†).

To visualize the crack formation, we image an 0.3 μL suspension drop with initial volume fraction ϕ = 22% on an inverted microscope using an objective of magnification M = 4× (Eclipse TE2000-U, Nikon). The drop is deposited through a removable window on a clean glass slide placed in a transparent environmental chamber with relative humidity that is controlled using either silica gels (Fischer Scientific) or saturated salt solutions (Sigma-Aldrich). After a partial receding of the liquid cap, radial cracks appear with avalanche-like dynamics,[22] as shown in Fig. 1b (Movie S2, ESI†). The cracks reach the center of the deposit when the liquid cap has fully evaporated, and the petals that are formed bend to create a flower-like shape;[12,14,23,24] at high volume fraction, the coffee ring observed in the dilute regime ''blooms''. How does such a spectacular transition of the pattern occur upon a change in particle volume fraction?

To investigate this transition, we vary the particle volume fraction ϕ from 0.04% to 22%. At ϕ = 0.04%, we observe the well-known coffee-ring effect characteristic of dilute colloidal suspensions,[16,17,25–27] as shown in Fig. 2a. The particles are brought towards the pinned contact line by an evaporation-induced flow in the drop, where they form a thin ring-shaped deposit.[16,17,27] The central part of the drop contains almost no particles and no clear pattern of cracks is visible in the deposit. As the volume fraction is increased to ϕ = 0.75%, a ring pattern remains,[28,29] as seen in Fig. 2b. However, this ring fractures into a large number of radial cracks which propagate with avalanche-like dynamics (Movie S3, ESI†). The central part of the drop remains almost particle free. We denote this regime as the ring-crack regime. Upon a further increase in volume fraction to ϕ = 1.7%, the deposit extends over the entire area initially wetted by the drop, as seen in Fig. 2c. Radial cracks form in an outer ring and eventually branch at a certain distance from the drop edge into a multitude of secondary cracks that propagate towards the center. We denote this regime the double-crack regime. While the cracks in the outer ring still exhibit an avalanching behavior,[30] the propagation of the branched cracks in the center is less controlled and multiple secondary cracks branch from a primary crack (Movie S4, ESI†). Above a critical volume fraction $\phi^* \approx 6\%$, cracks propagate to the center without further branching, as shown in Fig. 2d. We denote this as the single-crack regime. Remarkably, the three regimes of ring cracks, double cracks and single cracks are robust to an increase in the contact angle to $\theta = 40° \pm 2°$ (Fig. S1 and discussion in the ESI†) and to a change of the particle composition to polystyrene particles (Fig. S2 and discussion in the ESI†).

To quantify these different regimes of particle deposition, we determine the ratio w/R_0 between the crack length w and the initial drop radius R_0. In the double-crack regime, we only consider the outer set of cracks, as the secondary cracks in the center exhibit a different propagation mechanism than the avalanching dynamics observed for the main cracks. In the ring-crack regime and the double-crack regime, an increase in volume fraction leads to a monotonic increase of the normalized crack length w/R_0, with $w/R_0 = 0.16\sqrt{\phi}$, as shown in Fig. 2e. For the ring-crack regime, w also corresponds to the width of the ring deposit. A similar scaling of the ring width with the volume fraction has been reported in the coffee-ring regime[25,28] by considering conservation of mass of the particles and equating the final particle volume in a thin ring $w \ll R_0$ of maximum thickness h and particle packing fraction ϕ_p with the initial particle volume, which yields $\phi_p h R_0 w \sim \phi {R_0}^3$, and thus $hw/{R_0}^2 \sim \phi/\phi_p$. With the theoretically predicted scaling of $h \sim w$ in the coffee-ring regime,[31] this indeed gives $w/R_0 \propto \sqrt{\phi}$. It is notable that this dependence extends into the double-crack regime, which suggests that the majority of the particles are deposited in the outer annular area of the pattern.

Remarkably, in the double-crack regime the width of the outer ring does not increase beyond 40% of the drop radius: the cracks stop branching into secondary cracks at a critical volume fraction ϕ^* = 6.3% ± 0.4%, denoting the transition between the double-crack and the single-crack regime. Within a transitional range

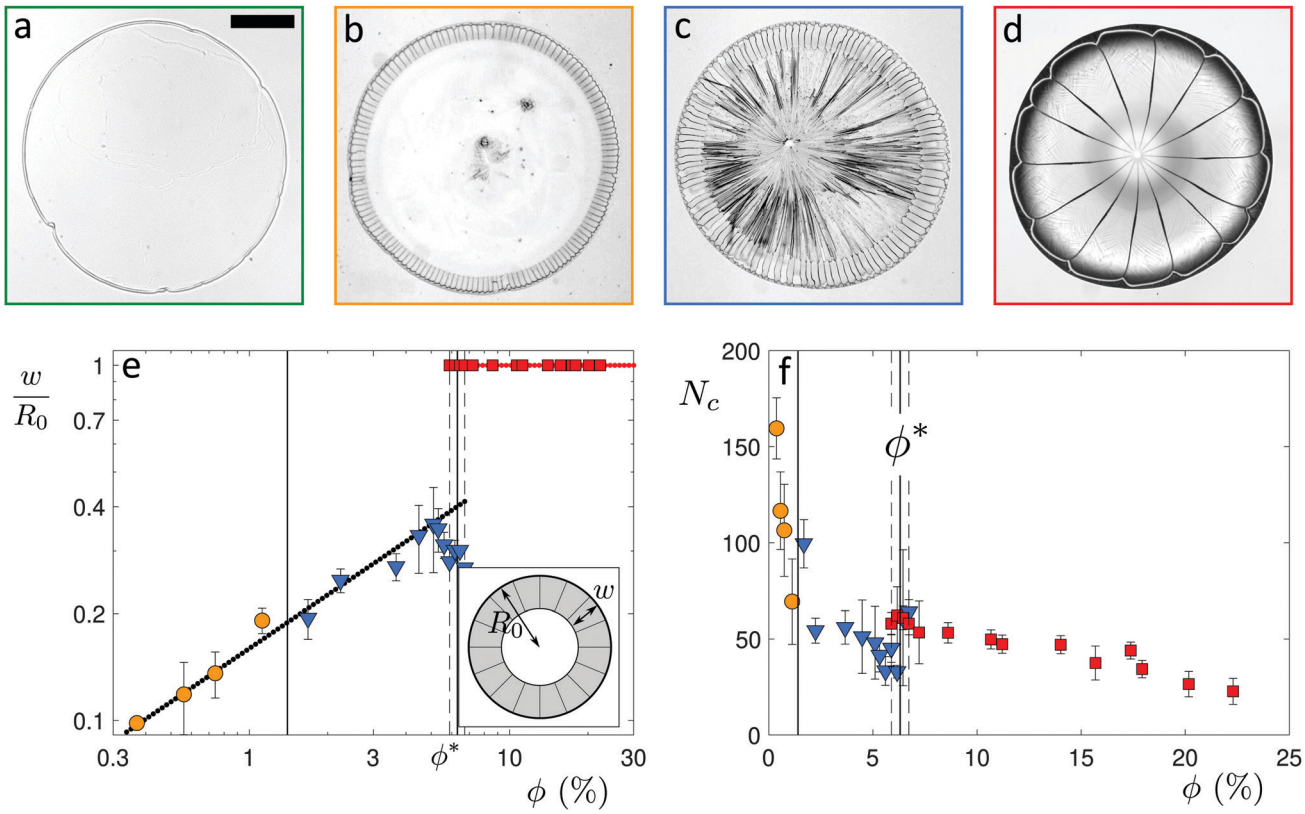

Fig. 2 Particle concentration as a control parameter for drying patterns. (a–d) Bottom-views of the final deposits formed by 0.3 μL suspension drops with initial volume fractions ϕ. The scale bar represents 500 μm. (a) At ϕ = 0.04%, a coffee ring forms. (b) At ϕ = 0.75%, a ring of radially-oriented cracks forms in the deposit. (c) At ϕ = 1.7%, double cracks form, where cracks on the outer ring branch into secondary cracks in the central area. (d) At ϕ = 22%, single cracks propagate from the drop edge towards the center. (e) Crack length w normalized by the initial drop radius R_0 *versus* the initial particle volume fraction ϕ. Above the critical volume fraction ϕ^*, $w = R_0$ in the single-crack regime (red squares). Below ϕ^*, $w/R_0 = 0.16\sqrt{\phi}$ (black dotted line) in the ring-crack (orange circles) and double-crack (blue triangles) regimes. Inset: Definition of the crack length w and the initial drop radius R_0. (f) Number of cracks N_c in the outer part of the deposit *versus* the initial volume fraction ϕ. The number of cracks decreases with ϕ in all regimes.

(5.9% $\leq \phi \leq$ 6.7%), both double cracks and single cracks are observed as the branching process varies slightly from one drop to another, which is in line with the larger error bars in this range. The discontinuous increase in crack length w/R_0 provides a signature of the transition from annular to discoidal deposits.

The number of cracks, N_c, decreases with increasing initial volume fraction in the ring-crack and double-crack regimes, as shown in Fig. 2f. We here consider the number of cracks in the outer ring of the double-crack regime. Approaching the boundary to the single-crack regime, the number of cracks exhibits a slight dip; within the transitional range around ϕ^*, N_c is systematically lower for double cracks than for single cracks, suggesting a discontinuous change in the number of cracks at this transition. Finally, for discoidal deposits in the single-crack regime, N_c decreases upon a further increase in ϕ (see also Fig. S3 in the ESI†). The decrease in the number of cracks with increasing volume fraction provides an opportunity to controllably tune the crack morphology.

Deposit thickness controls number of cracks

The distinct regimes of pattern morphology are due to a change in the shape of the deposit. We measure the height profile of the deposit along the radial direction during drying using a laser scanning confocal microscope (VK-X 3D, Keyence). By superimposing a sequence of images captured after the liquid cap receded, but before cracking and bending occur, we reconstruct the profile over a significant part of the drop, as shown in Fig. 3a, where we report the height z of the deposit as a function of the distance l to the contact line (located at $l = 0$) for drops of various initial volume fractions ϕ. At low volume fraction, in the ring-crack regime, the deposit thickness increases to a maximum thickness before decreasing to a non-measurable value at a length l = 80 μm. This length is in good agreement with that measured *via* microscopy, w, which confirms that the majority of the particles are indeed deposited within this ring. With increasing ϕ in the double-crack regime, the length of the ring grows systematically larger and the thickness of the deposit increases. The ring remains well-defined and the transition from the outer ring of cracks to the branching inner cracks coincides with the decrease of the deposit thickness to a much lower value, which indicates that branching is initiated by a decrease in deposit thickness. At large volume fractions in the single-crack regime, the deposit thickness increases with l until reaching a maximum; the

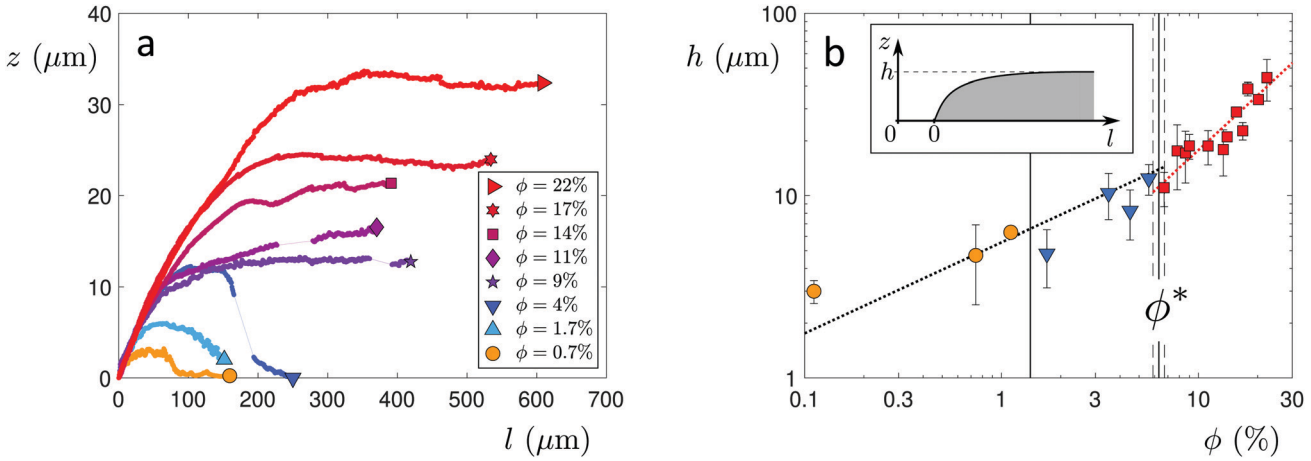

Fig. 3 Radial profile of the particle deposit. (a) Height z of the deposit along the drop radius (R_0 = 1 mm), where l is the distance from the contact line (l = 0). At particle volume fractions $\phi < \phi^*$ = 6.3%, the majority of particles are deposited in an outer ring. In the single-crack regime at $\phi > \phi^*$, the deposit reaches a maximum height and remains approximatively constant at larger l. (b) Maximum deposit height h *versus* initial particle volume fraction ϕ. The red dotted line represents a fit of the data in the single-crack regime to $h = (\phi/\phi_p)(\Omega/\pi R_0^2)$, which gives a packing fraction ϕ_p= 53.7%. The black dotted line denotes $h = (\phi/\phi_p)(\Omega/\pi R_0^2)(R_0/2w)$, with ϕ_p = 53.7% and $w/R_0 = 0.16\sqrt{\phi}$. Inset: Definition of the maximum height h and the coordinate l.

thickness then remains approximately constant at larger l within the range investigated.

We extract the maximum thickness h as an approximate measure of the deposit thickness. In the single-crack regime, h increases linearly with ϕ, in agreement with a roughly uniform particle coverage of the entire initially wetted area, as shown in Fig. 3b. Indeed, we can estimate the thickness by equating the volume of particles deposited at a particle packing fraction ϕ_p in a uniform deposit of thickness h to the volume of particles initially present in a drop of volume Ω, which yields $\pi R_0^2 h = (\phi/\phi_p)\Omega$. Fitting the measured thickness h to a linear relationship with ϕ provides an estimate of the particle packing fraction in the deposit of ϕ_p = 53.7%. This value is lower than the packing fraction corresponding to random close-packing, however, we here overestimate the deposit volume by taking the maximum thickness h as the measure of the deposit thickness. In the ring-crack and double-crack regimes, mass conservation of particles yields $hw/R_0^2 \sim \phi/\phi_p$ where we neglect the small fraction of particles present within the inner part of the drop. As $w/R_0 \propto \sqrt{\phi}$ in these two regimes, we expect $h \propto \sqrt{\phi}$. Using $w/R_0 = 0.16\sqrt{\phi}$ from the fit to the microscopy data leads to a satisfactory agreement with the deposit thickness measured in profilometry when using the value ϕ_p = 53.7% obtained in the single-crack regime, as shown by the black dotted line denoting $h = 5.56\sqrt{\phi}$ in Fig. 3b.

The particle volume fraction thus governs the deposit thickness, which in turn sets the number of cracks (Fig. S4 in the ESI†). This finding is in agreement with observations in various other geometries, including rectangular capillary cells and thin particle films, where thinner deposits have been reported to form more closely spaced cracks.[3,4,21,32,33] It also complements observations from experiments performed on substrates with different wettability that show that the number of cracks increases for drops with decreasing contact angle for $\theta < 90°$, due to the more extensive spreading of the liquid drop at smaller contact angles which leads to thinner deposits.[22,34,35] Even further evidence is provided in the double-crack regime where the density of cracks increases concomitantly with the decrease in deposit thickness at a distance w from the deposit edge. At very low volume fraction, the deposit thickness becomes thinner than the critical thickness needed to form a crack, which accounts for the absence of cracks in the coffee ring patterns. An energy balance between the elastic energy released upon crack formation and the incremental cost in total interfacial energy associated with crack formation yields a critical tensile stress which becomes larger for thinner deposits.[36] When this critical stress exceeds the tensile stress caused by the maximum capillary pressure due to the liquid meniscus between particles, air invades the deposit before a crack forms.[6,37] For a Ludox suspension with particles of diameter 22 nm, the critical deposit thickness below which no cracks form has been experimentally determined to be $h_c \approx$ 1 μm.[37] By extrapolating our measured deposit heights in the ring-crack and double-crack regimes to lower ϕ, we reach $h_c \approx$ 1 μm at $\phi \approx$ 0.03%, which is indeed in good agreement with the transition to the coffee-ring regime.

The dynamics of the deposit formation is set by the liquid cap retraction, which is governed by the drying time τ_d. To test whether the drying dynamics alters the deposit shape and crack morphology, we vary τ_d in two ways: (i) we probe a range of relative humidities from 15% to 75% corresponding to a variation in drying times by a factor of ~6, and (ii) we probe a range of initial drop volumes from 0.3 μL to 5 μL corresponding also to a variation in drying times by a factor of ~6. Increasing the drop volume increases the drop radius R_0, and thus the drop perimeter. However, we find that neither changing the relative humidity nor changing the drop volume has a noticeable influence on w/R_0 and N_c (Fig. S5 in the ESI†), which suggests that the crack spacing increases linearly with R_0,

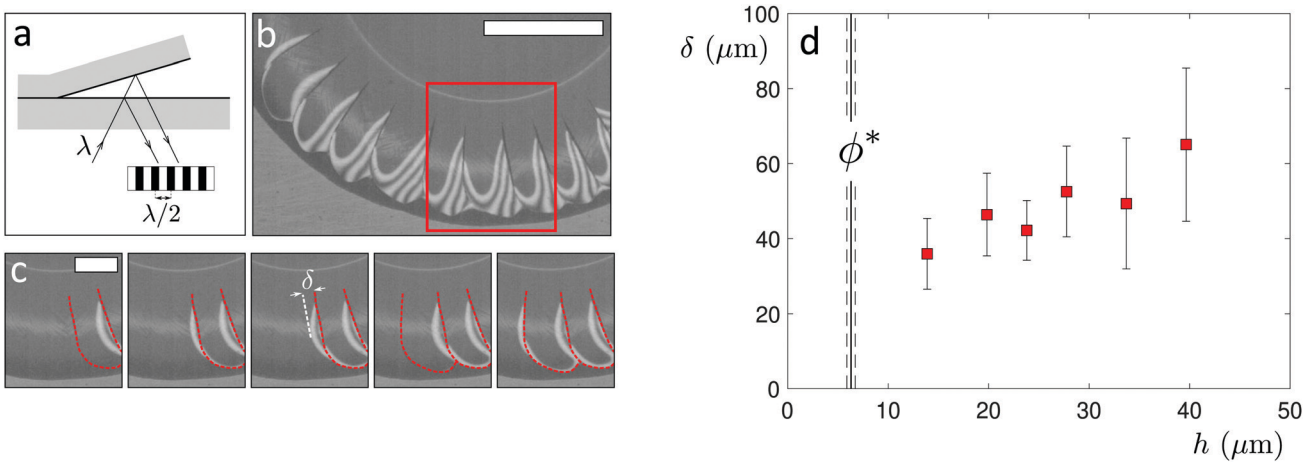

Fig. 4 Delamination leads to avalanche-like crack propagation. (a) Schematic of the interference setup (wavelength λ = 534 nm) used to identify the air layer between the glass substrate and the particle deposit. (b) Interference image of a section of a drop with initial volume fraction ϕ = 22%. After cracking, the deposit delaminates from the substrate and bends sideways away from the crack, which induces an avalanche-like crack propagation. The scale bar is 500 μm. (c) Image sequence with timesteps of 600 ms. The distance δ denotes the extent of the delamination at the moment a new crack nucleates. The red lines denote the cracks, the white fringes are interference fringes. The scale bar represents 200 μm. (d) The distance δ increases with the deposit thickness h for drops with different initial particle volume fractions in the single-crack regime. The distance δ and the deposit thickness h are of same order of magnitude.

maintaining the geometrical similarity of the pattern over the range of R_0 probed, and shows that the drying time is not a control parameter for the crack morphology. Likewise, the deposit shape remains unchanged upon a decrease in temperature by 5 °C, as shown in Fig. S6 in the ESI.†

Delamination as a precursor for crack propagation

Once a first crack has appeared, a subsequent crack forms from the previous one, propagating circumferentially along the deposit edge for a certain distance before turning again towards the drop center. This leads to an avalanche-like crack dynamics that propagates around the circumference of the drop,[22] which is observed in all three crack regimes. To reveal the origin of these dynamics, we visualize the crack formation with high-speed interference microscopy (Phantom Miro 320S, Movie S5, ESI†), which allows us to determine the air-layer thickness as the deposit delaminates from the substrate and bends upwards,[12,20,23,32] as shown in Fig. 4a–c. The deposit lifts laterally from a newly-formed crack, as evidenced by the appearance of interference fringes seen in the time sequence in Fig. 4c. The delaminated region grows in time and reaches a distance δ from the crack before the next crack forms. Notably, δ increases with the deposit thickness h, as shown in Fig. 4d for drops with different initial volume fractions ϕ in the single-crack regime. It is interesting to note that this delamination characteristic is reminiscent of that observed in the regime of limited decohesion in elastic sheets.[38] Moreover, delamination in elastic sheets similarly allows for collaborative fracture modes between propagating cracks that induce regular patterns whose characteristic spacing is governed by the film thickness.[39] A thin deposit of closed-packed particles thus, remarkably, shares some features with elastic solid films.

Conclusions

Our results reveal the rich variety of crack morphologies that can develop in drying drops of colloidal suspensions. We show that the particle volume fraction is the key control parameter that allows one to tune the particle deposition from a ring-like deposit to a deposit characterized by a thicker outer ring and a thinner interior deposit to a fairly uniform coverage of the entire, initially-wetted area. These deposits experience material failure through an avalanche-like crack propagation mediated by deposit delamination. The spacing between neighboring cracks is governed by the deposit thickness, which is tunable by varying the initial particle volume fraction. This robust control over different crack morphologies and spacing opens new pathways towards self-driven, spontaneous patterning of substrates, which might be exploited as a design tool for thin materials in micro-fabrication processes.

Conflicts of interest

The authors declare no conflicts.

Acknowledgements

We thank Gustave Ronteix, David Rivas and Joel Marthelot for helpful discussions, and Emily Yin for preliminary experiments. G. S., T. N. and I. B. acknowledge support from MISTI France. P. L. and I. B. acknowledge support from the MIT Research Support Committee. P. B. and G. H. M. acknowledge support from Procter & Gamble through a gift to G. H. M.

References

1 J. Walker, *Sci. Am.*, 1986, **255**, 204–209.
2 A. Groisman and E. Kaplan, *Europhys. Lett.*, 1994, **25**, 415–420.
3 C. Allain and L. Limat, *Phys. Rev. Lett.*, 1995, **74**, 2981–2984.
4 K. A. Shorlin, J. R. de Bruyn, M. Graham and S. W. Morris, *Phys. Rev. E: Stat. Phys., Plasmas, Fluids, Relat. Interdiscip. Top.*, 2000, **61**, 6950–6957.
5 E. R. Dufresne, E. I. Corwin, N. A. Greenblatt, J. Ashmore, D. Y. Wang, A. D. Dinsmore, J. X. Cheng, X. S. Xie, J. W. Hutchinson and D. A. Weitz, *Phys. Rev. Lett.*, 2003, **91**, 224501.
6 W. Man and W. B. Russel, *Phys. Rev. Lett.*, 2008, **100**, 198302.
7 E. M. Kindle, *J. Geol.*, 1917, **25**, 135–144.
8 L. Goehring, *Philos. Trans. R. Soc., A*, 2013, **371**, 20120353.
9 S. Bohn, J. Platkiewicz, B. Andreotti, M. Adda-Bedia and Y. Couder, *Phys. Rev. E: Stat., Nonlinear, Soft Matter Phys.*, 2005, **71**, 046215.
10 L. Goehring, R. Conroy, A. Akhter, W. J. Clegg and A. F. Routh, *Soft Matter*, 2010, **6**, 3562.
11 F. Giorgiutti-Dauphiné and L. Pauchard, *J. Appl. Phys.*, 2016, **120**, 065107.
12 F. Parisse and C. Allain, *Phys. Fluids*, 1996, **8**, S6.
13 L. Pauchard, F. Parisse and C. Allain, *Phys. Rev. E: Stat. Phys., Plasmas, Fluids, Relat. Interdiscip. Top.*, 1999, **59**, 3737–3740.
14 F. Giorgiutti-Dauphiné and L. Pauchard, *Eur. Phys. J. E: Soft Matter Biol. Phys.*, 2018, **41**, 32.
15 W. Han, B. Li and Z. Lin, *ACS Nano*, 2013, **7**, 6079–6085.
16 R. D. Deegan, O. Bakajin, T. F. Dupont, G. Huber, S. R. Nagel and T. A. Witten, *Nature*, 1997, **389**, 827–829.
17 R. D. Deegan, O. Bakajin, T. F. Dupont, G. Huber, S. R. Nagel and T. A. Witten, *Phys. Rev. E: Stat. Phys., Plasmas, Fluids, Relat. Interdiscip. Top.*, 2000, **62**, 756–765.
18 F. Parisse and C. Allain, *J. Phys. II*, 1996, **6**, 1111–1119.
19 F. Parisse and C. Allain, *Langmuir*, 1997, **13**, 3598–3602.
20 A. Osman, L. Goehring, H. Stitt and N. Shokri, *Soft Matter*, 2020, **16**, 8345–8351.
21 W. P. Lee and A. F. Routh, *Langmuir*, 2004, **20**, 9885–9888.
22 F. Giorgiutti-Dauphiné and L. Pauchard, *Eur. Phys. J. E: Soft Matter Biol. Phys.*, 2014, **37**, 39.
23 F. Giorgiutti-Dauphiné and L. Pauchard, *Colloids Surf., A*, 2015, **466**, 203–209.
24 P. Lilin, P. Bourrianne, G. Sintès and I. Bischofberger, *Phys. Rev. Fluids*, 2020, **5**, 110511.
25 R. D. Deegan, *Phys. Rev. E: Stat. Phys., Plasmas, Fluids, Relat. Interdiscip. Top.*, 2000, **61**, 475–485.
26 H. Hu and R. G. Larson, *J. Phys. Chem. B*, 2002, **106**, 1334–1344.
27 Á. G. Marín, H. Gelderblom, D. Lohse and J. H. Snoeijer, *Phys. Rev. Lett.*, 2011, **107**, 085502.
28 H. Lama, M. G. Basavaraj and D. K. Satapathy, *Soft Matter*, 2017, **13**, 5445–5452.
29 H. M. van der Kooij, G. T. van de Kerkhof and J. Sprakel, *Soft Matter*, 2016, **12**, 2858–2867.
30 R. Mulka, A. Kujawska, B. Zajączkowski, S. Mancin and M. H. Buschmann, *Colloids Surf., A*, 2021, **623**, 126730.
31 Y. O. Popov, *Phys. Rev. E: Stat., Nonlinear, Soft Matter Phys.*, 2005, **71**, 036313.
32 V. Lazarus and L. Pauchard, *Soft Matter*, 2011, **7**, 2552.
33 P. Nandakishore and L. Goehring, *Soft Matter*, 2016, **12**, 2253–2263.
34 U. U. Ghosh, M. Chakraborty, A. B. Bhandari, S. Chakraborty and S. DasGupta, *Langmuir*, 2015, **31**, 6001–6010.
35 N. Yan, H. Luo, H. Yu, Y. Liu and G. Jing, *Colloids Surf., A*, 2021, **624**, 126780.
36 A. A. Griffith, *Philos. Trans. R. Soc. London, Ser. A*, 1921, **221**, 163–198.
37 K. B. Singh and M. S. Tirumkudulu, *Phys. Rev. Lett.*, 2007, **98**, 218302.
38 H. M. Jensen, J. W. Hutchinson and K. Kyung-Suk, *Int. J. Solids Struct.*, 1990, **26**, 1099–1114.
39 J. Marthelot, B. Roman, J. Bico, J. Teisseire, D. Dalmas and F. Melo, *Phys. Rev. Lett.*, 2014, **113**, 085502.